

THRaws: A Novel Dataset for Thermal Hotspots Detection in Raw Sentinel-2 Data

Gabriele Meoni^{*}, Roberto Del Prete^{*}, Federico Serva^{*}, Alix De Beusscher^{*},
Olivier Colin[†], Nicolas Long  p  ^{*}

^{*} Φ -lab, European Space Research Institute (ESRIN), European Space Agency (ESA), Via Galileo Galilei, 1,
00044 Frascati RM (Italy)

[†]Copernicus & Ground Segment / Data Management Division, European Space Research Institute (ESRIN),
European Space Agency (ESA), Via Galileo Galilei, 1, 00044 Frascati RM (Italy)

Abstract—Nowadays, most of the datasets leveraging space-borne Earth Observation (EO) data are based on high-end levels products, which are ortho-rectified, coregistered, calibrated, and further processed to mitigate the impact of noise and distortions. Nevertheless, given the growing interest to apply Artificial Intelligence (AI) onboard satellites for time-critical applications, such as natural disaster response, providing raw satellite images could be useful to foster the research on energy-efficient pre-processing algorithms and AI models for onboard-satellite applications. In this framework, we present THRaws, the first dataset composed of Sentinel-2 (S-2) raw data containing warm temperature hotspots (wildfires and volcanic eruptions). To foster the realisation of robust AI architectures, the dataset gathers data from all over the globe. Furthermore, we designed a custom methodology to identify events in raw data starting from the corresponding Level-1C (L1C) products. Indeed, given the availability of state-of-the-art algorithms for thermal anomalies detection on the L1C files, we detect such events on these latter and we then re-project them on the corresponding raw images. Additionally, to deal with unprocessed data, we devise a lightweight coarse coregistration and georeferencing strategy. The developed dataset is comprehensive of more than 100 samples containing wildfires, volcanic eruptions, and event-free volcanic areas to enable both warm-events detection and general classification applications. Finally, we compare performances between the proposed coarse spatial coregistration technique and the SuperGlue Deep Neural Network method to highlight the different constraints in terms of timing and quality of spatial registration to minimise the spatial displacement error for a specific scene.

Index Terms—Onboard AI, Raw dataset, Sentinel-2, Volcanic Eruption, Wildfire.

I. INTRODUCTION

THE capability of Artificial Intelligence (AI) algorithms to extract actionable information from Earth Observation (EO) satellite data has motivated research on their operational use directly onboard spacecraft [1]. The use of AI onboard satellites constellations is, in fact, now being explored to provide near-real-time response for wildfires [2], oil spills [3], volcanic eruptions [4], [5], floods [6] and other catastrophic events [2], [7], [8]. Furthermore, the application of AI onboard satellite has been proved effective to reduce downlink data-rates by enabling preventive filtering of cloud-covered or corrupted data [9], [1] or higher image compression rates [10]. While the complexity of models deployable onboard is definitely increased [1] over time, thanks also to the possibility

to exploit energy-efficient Commercial Off-The-Shelf (COTS) components, very few concerns have been raised for treating raw data.

Most of the relevances were demonstrated on high-level satellite optical products [4], [5], [8], [6], which exploit calibrated, ortho-rectified, and further processed images to lower the amount of noise in the processing chain. Since these applications are deployed on the ground, they are hardly optimised for onboard purposes. Indeed, being computationally intensive, the implementation of the standard processing chain is prohibitive on nano-satellites (nano-sats). Furthermore, despite micro and mini-sats generally having increased computing capabilities compared to nano-sats, the optimisation of preprocessing steps is of utmost importance to reduce the need for additional specific hardware and to allow for higher mission duty-cycles.

The paper configures itself in this framework, closing this gap in the literature by proposing for the very first time a raw multi-spectral dataset together with a methodology to reference and geo-locate the spectral bands. The developed THRaws (Thermal Hotspots in Raw Sentinel-2 data) is constituted of a collection of raw images of warm temperature hotspots. We focus our attention on wildfires and volcanic eruptions because this application has the potential to enhance early warning systems and prevent fires from spreading and causing further destruction [5], [2]. Additionally, onboard hotspot detection can contribute to the safety and security of people in high-risk areas, as well as critical infrastructure such as power lines and oil pipelines. It is crucial to note that the term “raw” data as we intend does not exist, as the Level-0 (L0) products are compressed in the Instrument Source Packet (ISP) format. In the present manuscript, we refer to “raw” as the data that better represent the ones gathered by an onboard multi-spectral sensor (as better detailed in Sec. II-C).

To summarize, the contribution of our work is two-fold. From one side, we developed a methodology to design datasets for the detection of thermal hotspot events on raw Sentinel-2 data. Despite being conceived for the detection of thermal hotspots events, the proposed approach is widely applicable for the design of any classification/detection tasks on Sentinel-2 raw data. From another side, we model a lightweight “coarse

spatial coregistration” and georeferencing methodology¹ that is fast but provides a sufficient accurate spatial registration to locate events on L0 data after detection on Level-1C (L1C) data. This is necessary since Sentinel-2 raw data are unregistered and not georeferenced. As for [11], the coarse spatial registration algorithm exploits one-time precalculated spatial shifts to compensate the average spatial displacements both along and across the satellite-track due respectively to the pushbroom nature of the sensor and additional sensor offsets. This calibration approach does not require the use of ground control points or ancillary data. We also compared the proposed methods with respect to a solution providing values of spatial shifts optimised for a single image in terms of timing and accuracy. Our findings encourage further studies envisioning the proposed method as a solution that can be used for onboard satellite usage.

The remainder of the paper is organised as follows. Section II discusses the standard processing chain of Sentinel-2 product data. Section III provides a State-of-the-art analysis of common methods used to preprocess raw data used for current missions leveraging AI onboard EO data. Section IV offers an overview of the proposed dataset creation methodology, of which Section V outlines the solutions adopted to select and download data, whilst Section VI illustrates the processing steps to filter and process data. Furthermore, it presents our custom lightweight spatial coarse spatial coregistration methodology. Section VII presents the results in terms of the number of identified decompressed L0 granules. This section also highlights the performance achieved by our coarse coregistration technique. Benchmarks on different devices provides meaningful insights into the effectiveness of our approach. Finally, Section VIII draws the conclusion of this work.

II. SENTINEL-2 MISSION & DATA PROCESSING

A. The Sentinel-2 mission

The Sentinel-2 mission is part of the Sentinel constellation and comprises two identical satellites, Sentinel-2A (S2A) and Sentinel-2B (S2B), providing 5 days revisit time at the equator with a wide swath (290 km) and each carrying the high spatial resolution Multi-Spectral Instrument (MSI) sensor [12]. MSI measures the Earth’s radiance in 13 visible (VIS) and shortwave infrared (SWIR) bands with a spatial resolution between 10 and 60 m and the sensor acquires data in a pushbroom imaging mode in sun-synchronous orbit (SSO). The mission provides near-global coverage of land areas, the Mediterranean and closed seas, and coastal waters globally. The Sentinel-2 archive comprises data since 2015 for S2A and from since 2017 from S2B, with data usability for surface monitoring limited by the presence of clouds, as for other optical sensors.

B. The Sentinel-2 sensor

The payload consists of 12 detectors arranged in a staggered array perpendicular to the flight direction of the satellite.

¹The proposed methodology can be reproduced through *PyRawS* (Python for RAW Sentinel-2 data), a python library to handle Sentinel-2 decompressed raw products: <https://github.com/ESA-PhiLab/PyRawS>

Acquiring in a pushbroom configuration, each detector has 13 spectral bands [13], [14]. The detectors capture light reflected from the Earth’s surface in narrow strips, or “swaths,” as the satellite moves forward, which are then combined to create an entire scene.

Bands B02, B03, B04 correspond to blue, green and red colours, whilst B08 has a broadband response in the Near-InfraRed (NIR). These spectral bands have 10 m spatial resolution in the L1C products. B05, B06, B07, B8A are 20 m spatial resolution bands that cover various sub-portions of the NIR spectrum with a narrower bandwidth than B08. B10, B11, B12 are spectral bands in the SWIR. B11 and B12 have 20 m spatial resolutions, whilst B10, together with B9 (NIR) and B1 (visible) offer 60 m spatial resolution and can be used to quantify respectively cirrus cloud, water vapour and coastal aerosol properties.

C. Sentinel-2 processing chain

Sentinel-2 reflectance data are provided to the users either as L1C top-of-atmosphere (TOA) or L2A Bottom-Of-Atmosphere (BOA) atmospheric-corrected values [12]. For onboard processing applications it is, however, meaningful to focus on L1C products [15], since the atmospheric correction step involves computationally intensive processors, and may thus also benefit from Deep Learning (DL) approaches [16].

The processing chain of Sentinel-2 data is schematically shown in Fig. 1 and can be summarised as follows. Sensed data in a given acquisition are organised into *granules* for the area imaged by each detector in a 3.6 s period [14]. Since the satellite is operating in pushbroom mode, a granule contains all the data acquired by each sensor, but still not spatially coregistered.

Data produced by the sensor are equalized and compressed onboard the satellites before the downlink. This represents the L0 product. After the download, L0 data are, first, processed to produce metadata, including geographical information, a quicklook and other ancillary information.

The L0 data, with additional metadata, are decompressed. In the frame of this paper, the data obtained at this point of the processing is referred to as the **raw** data. It should be noted that this data has undergone on-board a process of equalization prior to compression [12], which aims at minimizing the effect of the wavelet-based compression algorithm on the accuracy/integrity of the raw detector measurements restituted after decompression on-ground. Level-1A (L1A) products are then generated by applying a coarse coregistration step. Our **raw** data corresponds to the products in the processing chain after the decompression of L0 data with additional metadata.

After that, L1A data processed to calculate radiometrically corrected radiances through various processing steps that include, among the others, the inversion of onboard equalization. In addition, the radiometric corrected geometric model is refined and appended to the radiometric corrected L1A data to produce Level-1B (L1B) products.

Finally, L1C data are then obtained from L1B products after geometric corrections, which include sub-pixel multispectral spatial registration, ortho-rectification and calculation of TOA

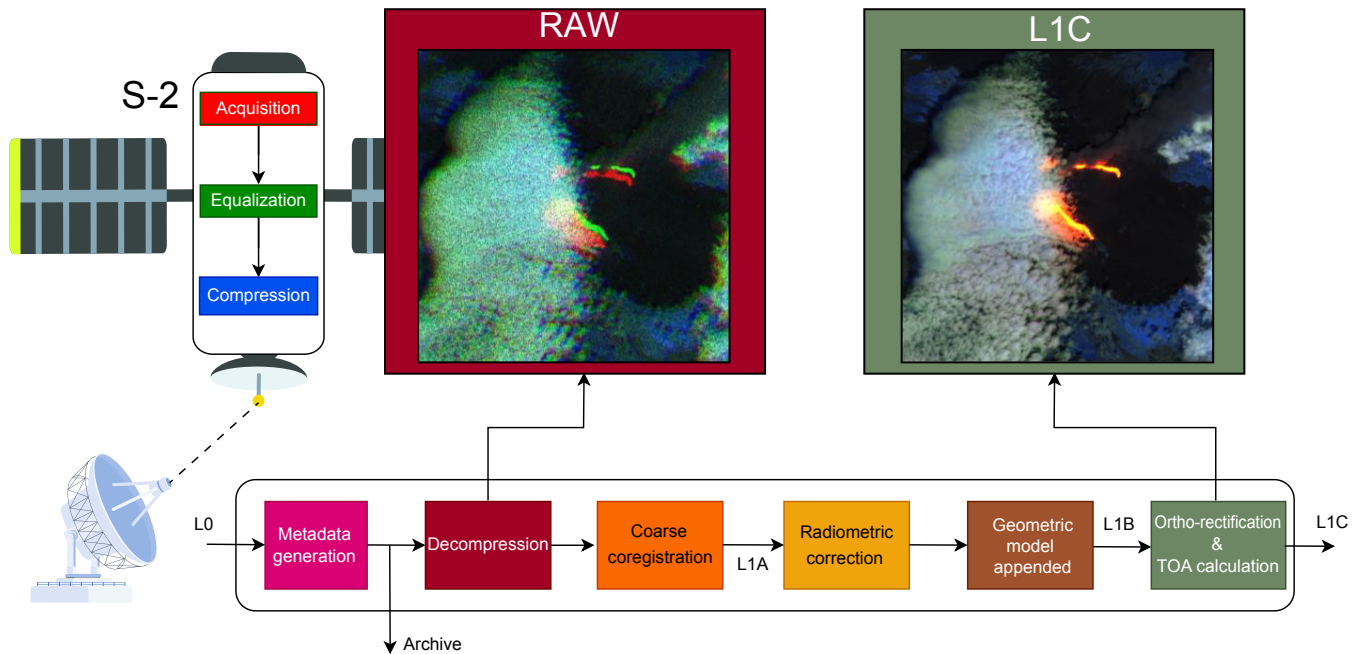


Fig. 1. Illustration of the processing chain from satellite data to L1C data. The images in the raw and L1C format show an eruption of the Etna volcano, Italy, for the two processing levels.

reflectances. Cloud and land masks are also generated within this step. To ensure high-quality products, various geometric and radiometric periodic calibration activities are performed, as detailed in [17]. Note that L1C products are delivered for predefined $100 \times 100 \text{ km}^2$ tiles, and a given acquisition may have partial or complete data coverage of an Area Of Interest (AOI). Therefore, when needed we mosaic multiple L1C tiles to cover the whole L0 AOI.

The entire processing chain is shown in Fig. 1. Note that until now the products in the chain from Raw to L1B included have not been available to users at the time of writing, while L1C, atmospheric-corrected BOA Level-2A data as well as higher level derived products for different domain applications, such as marine ecosystem monitoring² and land cover/land use assessment³ are also available from Copernicus and ESA projects. Therefore, products beyond the L1C processing level are not in the scope of this work.

III. STATE OF THE ART ANALYSIS

This section reviews the various approaches for processing raw optical data used in previous missions. For optical RGB data, some previous works investigated the feasibility to process the raw sensory data directly by using DL or Machine Learning (ML) algorithms without intermediate processing steps. One of these works is “The OPS-SAT case” [18], a data-centric competition hosted by the European Space Agency (ESA) Kelvins platform investigating few-shot learning for onboard satellite applications [19]. The competition was based on the images produced by OPS-SAT

satellite, which is equipped with $80\text{m} \times 80\text{m}$ resolution RGB camera [20]. During the competition, participants were asked to train an EfficientNet-lite0 model [21] to classify unprocessed sub-portions of the images into 8 classes. Competitions materials included 26 raw 2048×1944 pixels images, cropped into 200×200 patches, whose only 10 patches per class were labeled to investigate few-shot learning for onboard satellite applications.

The WildRide mission [22] proposes the onboard adoption of *WorldFloods*, a Deep Neural Networks (DNN) to detect floods from a miniaturized RGB camera. The study aims to demonstrated that onboard AI can dramatically decrease the time required to broadcast flood maps via a large decrease of data volume, from raw EO images to flood insight delivered as vector file format. The *WorldFloods* models have been previously trained on Sentinel-2 L1C products by using all 13 bands.

The authors demonstrate the ability to operate on uncalibrated images from an onboard RGB camera, effectively adapting the model to new sensing instruments and addressing data-shift problems. Despite the *WorldFloods* was originally trained on Sentinel-2 L1C images, to obtain acceptable performance on the RGB images, which significantly differ in terms of radiometric and spectral resolution, the authors retrained the model on four acquisitions from the used RGB camera, which were manually labeled after deployment of the satellite. This underlines the importance to have available raw satellite image datasets for the training of AI models to take into account of the impact of the lack of calibration and other non-ideal effects affecting raw data.

Furthermore, whilst [22] claims that ML-inference times are

²<https://marine.copernicus.eu/news/may-2021-product-release-sentinel-2-and-3-improve-water-quality-monitoring>; last accessed, February 2023

³https://seom.esa.int/page_project025.php; last accessed, February 2023

consistent on several different hardware accelerators (NVIDIA Jetson Nano, Google Coral, Myriad X), they state that the timing required by pre-processing steps of Sentinel-2 such as the band-to-band alignment, radiometric calibration, and fine coregistration must be taken into account.

For what concerns multispectral and hyperspectral images, most of the works in literature implement a solution to pre-process the raw images onboard spacecraft before providing data as input to the AI models. Such solutions usually consist of simplified approaches to apply geometric and radiometric corrections compared to the ones performed on the ground. In the 6-U Φ sat-1 [9] CubeSat, which is the first satellite inferring a Convolutional Neural Networks (CNN) on a COTS edge device –i.e., the Intel-Movidius Myriad 2 Virtual Processing Unit (VPU) – to perform onboard pixel-level cloud-detection on the processing of three selected bands of the hyperspectral cube. The image processing chain limits the hyperspectral data-cube creation by performing coarse band-to-band spatial registration on three selected bands, sufficient to permit a CNN to create a cloud detection mask.

The HYPSON-1 (HYPER-spectral Smallsat for ocean Observation) is a CubeSat equipped with hyperspectral payload targeting the observation of ocean color to detect algal blooms along Norwegian coasts [23]. The hyperspectral image processing chain onboard HYPSON-1 uses the methodology described in [11], which implements radiometric and geometric corrections as linear operations. Correction matrices are one-time calculated after being calibrated through the use of granule-control points.

Since in many cases, the raw data is not made available as a product at the time of writing, as for Sentinel-2 missions, and since most of the previous missions adopting AI onboard satellites opted to infer their models on post-processed images, most of the current multi- and hyperspectral datasets and AI models target post-processed images [24], [5], [8], [6].

IV. OVERVIEW OF THE DATASET CREATION METHODOLOGY

The procedure to create the dataset is shown in Fig. 2. As a first step, we procured compressed raw data and L1C data containing volcanic eruptions, wildfires and not-events. To retrieve the dates and location of events we proceeded as described in Sec. V-A, V-B, V-C for the different classes. Then, we searched for available Sentinel-2 L1C products matching the dates and the location of interest.

To search for raw data, it was necessary to specify a polygon surrounding the AOI and a range of dates. This leads to download all the L0 *granules* whose reference band (B02) intersects the polygon and whose *sensing date* is included in that range. However, to select raw data correctly, it is necessary to consider that for a specific point the entire collections of the bands could be located in different granules before the spatial registration. Because of that, we first inspected L1C tiles to retrieve the coordinates of the events (i.e., volcanic eruptions and wildfires). Then, to ensure to collect all the bands for the events of interest we used a polygon of area $28 \times 10 \text{ km}^2$ centred at the coordinates of the events. The size was chosen because 14 km corresponds to the maximum along-track

distance commonly covered by all spectral bands reported in an MSI scene, which get, then, segmented into separate L0 granules. Therefore, since the satellite track approximately extends from north to south with a smaller error closer to the Equator, selecting a polygon that extends 14 km vertically toward north and south will ensure that all the bands for the centre of the download polygon –i.e., the centre of the eruption – will be downloaded. Furthermore, the width of 10 km^2 was sufficient to contain the warm temperature hotspots in the dataset.

Nevertheless, since the polygon is not perfectly oriented along the satellite track line and because the real AOI could be much smaller than the polygon, this procedure generally leads to download a higher number of raw data granules than required. Fig. 3 shows the granules downloaded (red rectangular shapes) for the volcanic eruption of Etna on 30/08/2021. The polygon used to specify the AOI is shown in white. But clearly only the raw data granules in yellow and pink actually contain the events.

For that reason, raw data granules were filtered to identify only the ones containing the warm temperature hotspot. To this aim, we used the methodology described in Sec. VI that selects the raw data granules containing warm temperature hotspots by processing L1C tiles that were mosaicked and cropped on the same area by using state-of-the-art algorithms. To ensure that all the necessary L1C tiles to match the raw data granules, we retrieved all the L1C products intersecting the polygon of interests.

After downlinking, raw data need to be decompressed to be readable. To this aim, we processed as described in Sec. V-D.

V. DATA SELECTION AND DOWNLOAD

A. Selection L1C tiles containing eruptions

The starting point for selecting tiles with eruptions is the Smithsonian Institution database [25], providing detailed information on global volcanism. From the database we selected only events occurring during the S2A launch until the time of writing, i.e. from 2016 to 2022, and we aimed at sampling different latitudes and seasons. From the database we only selected more intense and explosive eruptions, with volcanic explosive index (VEI) larger than 1, since effusive eruptions are less dangerous [26]. As events can last for several years, we originally selected up to three volcanic events for each eruption and up to three eruptions for a single location to ensure diversity of the dataset. However, during revision of the dataset, some raw data granules originally marked as not-events were found to contain volcanic thermal hotspots, leading to more than three volcanic events for some of the eruptions.

For shorter (days-months) eruptions, we selected acquisitions as close as possible to the event starting date to test the capability of detection in the early stages. From the list of eruptions, we visually inspected the candidate L1C tiles to confirm that the event was captured. For each of the selected L1C, we marked the location of volcanic event and used its coordinates as a centre of the rectangular polygon used to download raw data granules, as detailed in Sec. IV.

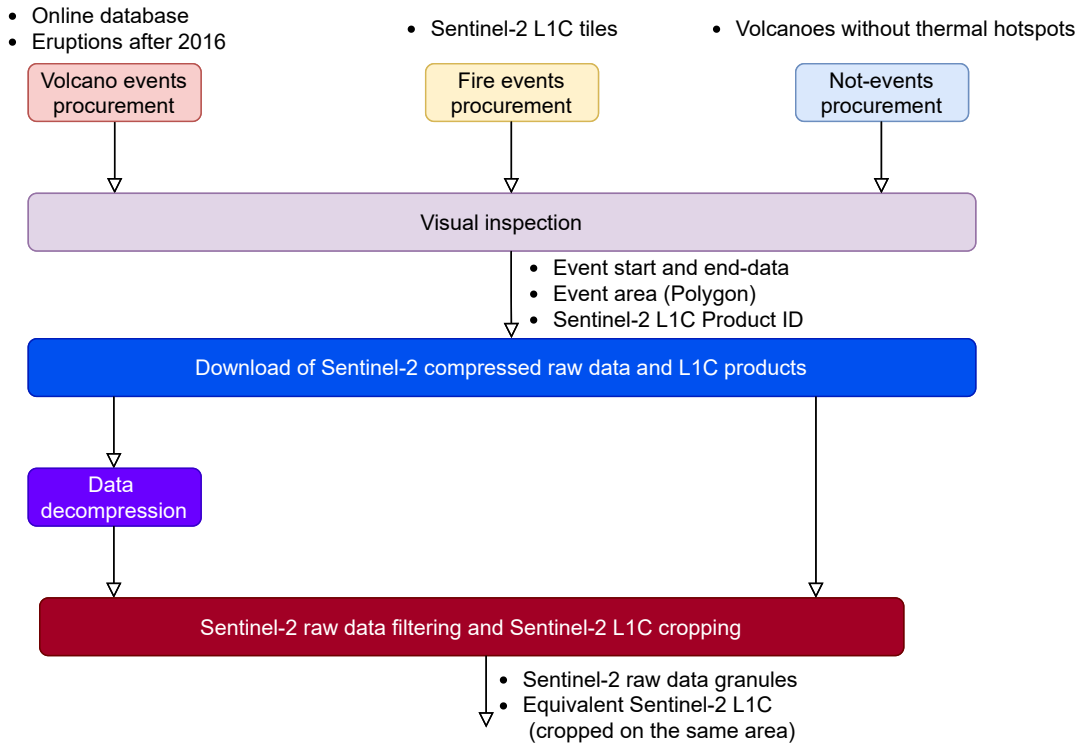


Fig. 2. Dataset creation methodology.

B. Selection of L1C tiles containing fires

Fire events are challenging to detect as they are shorter-lived, smaller and their locations are not known in advance compared to volcanic eruptions. We compiled a list of events starting from the Copernicus Emergency Monitoring System database⁴ and integrated the resulting list of events with real-time detection services⁵ and information available online from space and environmental agencies. Wildfires in vegetated areas are more likely during local afternoon, since air has warmed and the ground drier than in the morning hours [27]. Given the Sentinel-2 orbit characteristics, this implies that the database will mostly contain more severe and longer fire events. Moreover, wildfire hazards are more likely in areas where abundant biomass build-up in the wet season can be converted in fire fuel during the local dry season [26], such as in tropical countries. As for eruptions, candidate L1C acquisitions have been visually inspected to verify the presence of a fire front or extensive smoke. Finally, a number of fire events roughly equal to that of eruptions is retained to balance the dataset distribution.

C. Selection of Not-events

Hard negatives are introduced in the dataset to optimise model performances by a proper selection of Not-events. This approach aims at establishing consistent relationships between

thermal anomalies and network outputs as it enables the identification of specific anomalies in the image not necessarily related to volcanic eruptions, e.g., crater rim edges. The process of selecting not-events involves visually inspecting each granule and manually selection to ensure absence of hotspots. It is worth noting how this is important to allows for a more accurate ingestion of the data in DNN models.

D. Download and uncompression of L0 data

The L0 products were accurately selected and extracted from the long-term archives operated in the Copernicus Ground Segment. The compressed L0 image data in the products was then decompressed and translated in the form of raw TIFF single band images, each one corresponding to one spectral band and covering the field of view of a single MSI detector along one MSI scene (a so-called L0 granule), as sensed by the instrument prior to on-board compression. The set of so-obtained TIFF image granules is what is referred to as the "raw data granules". The raw data granules are then processed as described in Section VI to discard those not containing high thermal hotspots.

VI. DATA PROCESSING AND PREPARATION

A. Raw data granules filtering

As explained in Section IV, the methodology used to identify and download raw data can lead to the retrieval of raw data granules that do not contain warm temperature hotspots. Therefore, we developed the methodology shown in Fig. 4 to

⁴<https://emergency.copernicus.eu/mapping/list-of-activations-rapid>; last accessed, February 2023

⁵<https://firms.modaps.eosdis.nasa.gov/map>; last accessed, February 2023

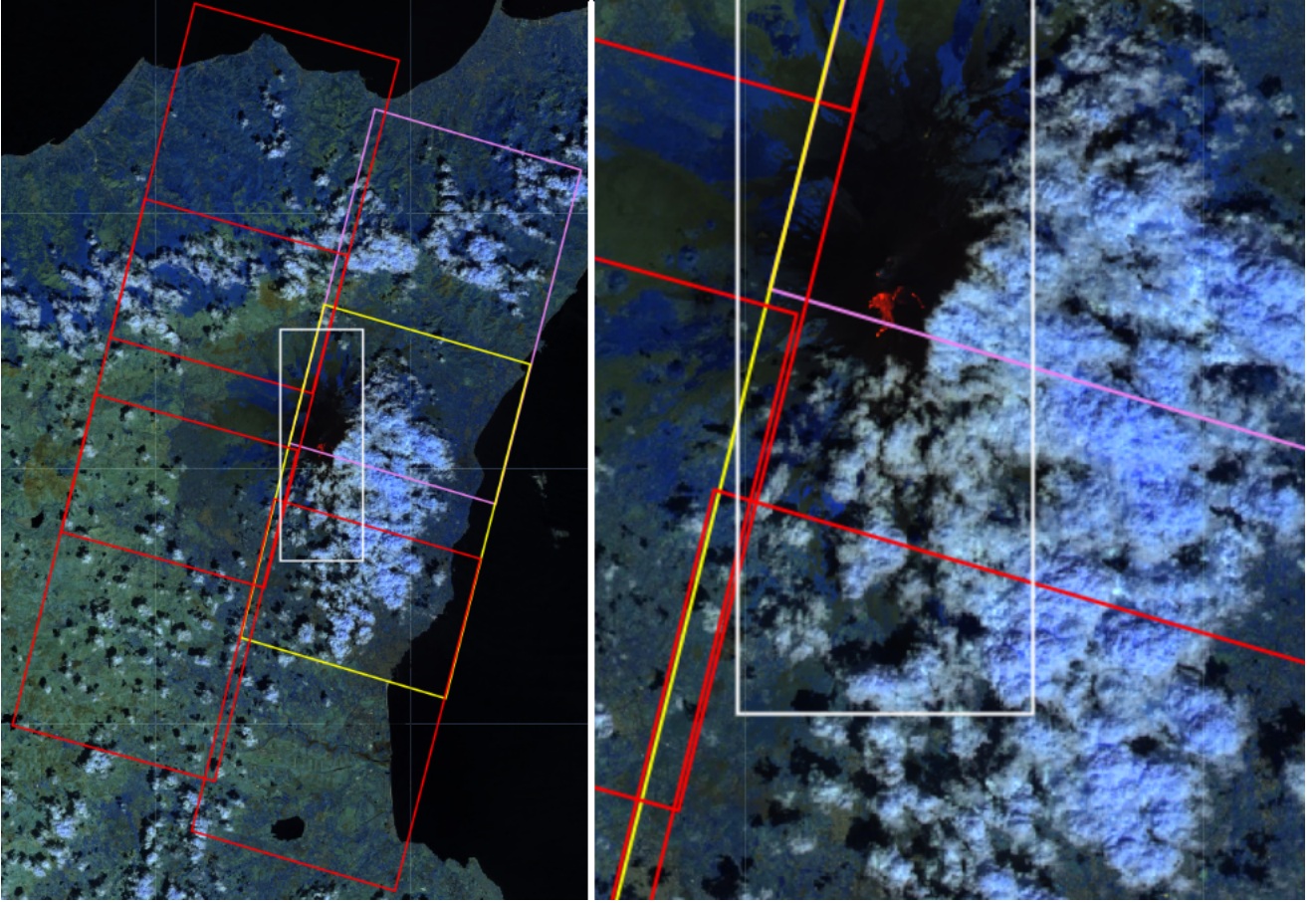


Fig. 3. On the left, the downloaded raw data granules (red, yellow and pink) are for a specific download polygon surrounding a volcanic eruption (white). On the right, a zoom on the volcanic eruption is displayed.

identify only the raw data granules of interest.

For brevity, the term "granule" will now be precisely referring to these raw data granules, as opposed to the more generic usage of the term in former paragraphs (e.g. such as in the data processing chain description of Sec. II-C). Despite our focus on warm temperature hotspots, the presented methodology is general and can be used for any object-detection/classification methodology. In particular, our approach consists in using the state-of-the-art algorithms that are available for LIC products to identify temperature hotspots by producing a bounding box and reprojecting them on the raw data granules. Granules not containing bounding boxes can be, therefore, discarded.

To this aim, it is first necessary to identify an algorithm that retrieves the desired event on LIC data. For warm temperature hotspots, we used a simplified version of the algorithm described by Massimetti et al. [28] to generate a mask selecting pixels containing warm-temperature anomalies. The algorithm is originally designed for volcanic events only, but our simplified implementation detects wildfires with sufficient accuracy. The various state-of-the-art algorithms usually exploits a subset of the 13 bands included in Sentinel-2 data. For our goal, we selected $B_S = [B_{8A}, B_{11}, B_{12}]$ used by the reference algorithm [28], which are also exploited by other state-of-the-art solutions with some possible additions.

Let us define $B_S \triangleq [B_x, B_y, \dots, B_z]$ the ordered list of the

bands used by the identified algorithm, where B_x is the first band of the collection. For each warm hotspot temperature event in the dataset, every granule is then processed as follows. First of all, we perform the *Coarse Spatial Coregistration (CSC)* of the different bands of B_S with respect to B_x . The CSC shifts all the bands of B_S except B_x along track and across track to match the area covered by the band B_x . The missing pixels due to the shift procedure could be cropped, filled by zeros or by pixels of adjacent granules when available. The technique and the concept of CSC is described in Sec. VI-B.

The shift of the various bands creates areas in which one or more bands are not available. Such pixels were filled with the area of adjacent granules when available or cropped when no adjacent granules are not available in the collection. The bands of the coregistered granule are then georeferenced. This is performed through the approach detailed in Sec. VI-C, since only the coordinates of the corners of the entire granule footprint are provided in the metadata of a granule, but not for the different bands [14]. After extracting the coordinates of the four vertices of the raw bands, it is now possible to crop LIC data on the same area of the first band of the collection B_x of the coregistered granule. However, the area of a raw band is not generally contained in a single LIC tile. Because of that, all the different LIC tiles intersecting the polygon

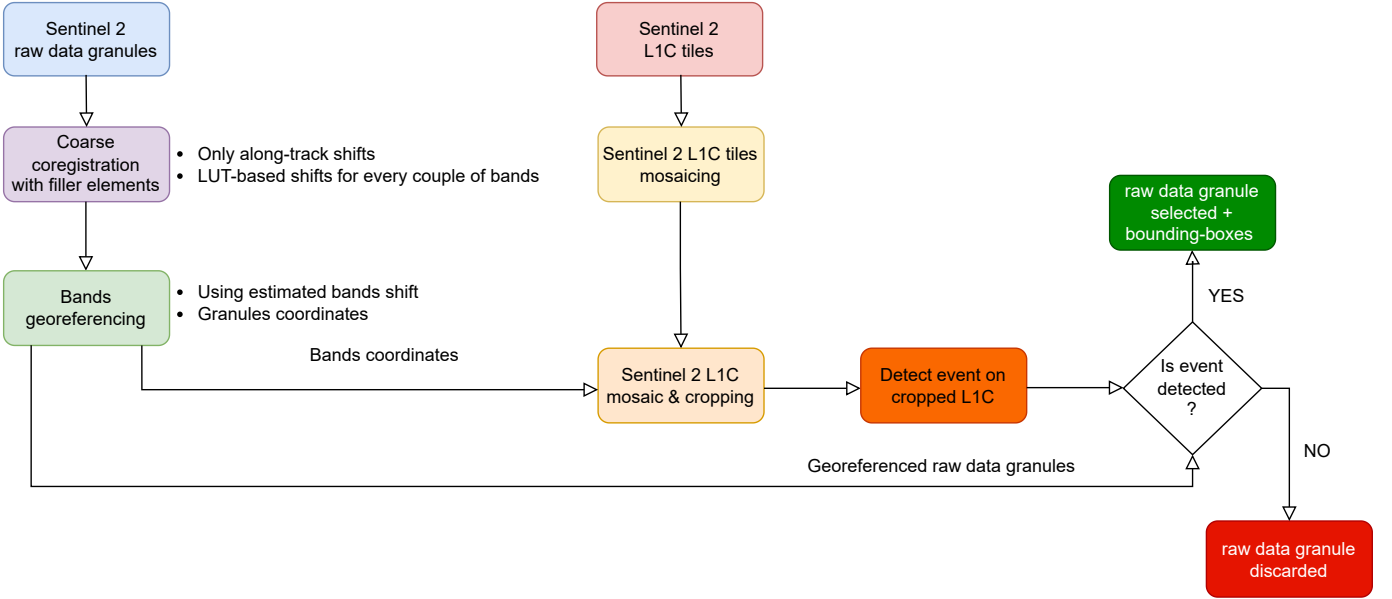


Fig. 4. Raw data granules filtering methodology. The selected bands of raw data granules are spatially coarsely registered and geo-referenced. The corresponding L1C tiles are mosaicked and cropped on the coordinates of the first band of the collection. Events of interest are then identified by applying a state-of-the-art algorithms and reprojected on the raw data granules. If not-event is identified, the raw data granule is discarded.

used to download for raw data are appropriately mosaicked and cropped on the same area of the band B_x .

After cropping these adjusted L1C tiles, they are processed to search for volcanic eruptions and wildfires by using the simplified implementation of the reference algorithm [28]. A bounding box is created on the L1C data for each event. When it is not possible to find a bounding box for a certain cropped L1C tile, the correspondent granule is discarded. Otherwise, the bounding boxes are warped back on the granule by using a linear transformation and then manually fine-tuned.

We define *Useful granule* a granule whose band B_x (B8A for our goal) includes at least a bounding box. It is necessary that this definition of *Useful granules* depends on the band collection used and, therefore, on the reference L1C algorithms used to retrieve the events of interest. In particular, our approach could discard granules including warm temperature hotspots that are not contained in the band B8A. For this reason, we provide the entire granule collections for each raw event to allow the users to label the raw data with reference algorithms using different bands collections, even if only *Useful granules* will be considered for the count of the raw data containing warm hotspot events.

The solutions conceived to process L1C tiles and to warp the event bounding boxes are respectively outlined in Sec. VI-E and Sec. VI-D.

B. Coarse Spatial Coregistration

Let us define I the the vector of band indices as shown in Eq. 1:

$$I \triangleq \{02, 08, 03, 10, 04, 05, 11, 06, 07, 8A, 12, 01, 09\} \quad (1)$$

I is sorted according to the time delays of the various bands compared to the band B_{02} [29]. Given two generic bands $B_{I(n)}$

and $B_{I(m)}$ of a granule, the band $B_{I(n)}$ is generally shifted of a certain number of pixels $S_{B_{I(n)}-B_{I(m)}}$ with respect to $B_{I(m)}$. $S_{B_{I(n)}-B_{I(m)}}$ is expressed with the resolution of the band $B_{I(n)}$. In general, it is possible assume that $S_{B_{I(n)}-B_{I(m)}}$ is made of two components as shown in Eq. 2:

$$S_{B_{I(n)}-B_{I(m)}} = \overline{S_{B_{I(n)}-B_{I(m)}}} + \Delta S_{B_{I(n)}-B_{I(m)}} \quad (2)$$

where $\overline{S_{B_{I(n)}-B_{I(m)}}}$ is the systematic shift due to push-broom acquisition mode and additional offset [14], whilst $\Delta S_{B_{I(n)}-B_{I(m)}}$ is an aleatory component due to mechanical vibrations and other non-ideal effects.

Spatial coregistration algorithms are generally designed to eliminate both the components of $S_{B_{I(n)}-B_{I(m)}}$ so that the spatial displacement between $B_{I(n)}$ and $B_{I(m)}$ can be minimised [30], [31]. In addition, they also eliminates errors in skewness, rotation, and warping [32].

However, spatial coregistration algorithms are computationally intensive and could require dedicated additional hardware to be implemented onboard satellites [9], [30], [31], [33]. In addition, as described in Sec. VII-B, for Sentinel-2 data $\overline{S_{B_{I(n)}-B_{I(m)}}} \gg \Delta S_{B_{I(n)}-B_{I(m)}}$, especially the component to compensate the shift along the satellite track (*along-track shift*). For this reason, in this work we propose a spatial coregistration solution designed to compensate only the systematic shift error component $\overline{S_{B_{I(n)}-B_{I(m)}}}$ by shifting B_m of a fixed value equal to $\overline{S_{B_{I(n)}-B_{I(m)}}}$. Given its limited precision, we call our coregistration solution a "CSC".

Despite the in the phase of dataset desing there are not the same limitations that in an onboard scenario, the use of CSC was preferred to more complex spatial coregistration solutions. Indeed, it does not affect the detection of warm temperature hotspots for our dataset whilst it speeds up the processing and the analysis of raw data, as shown in Section

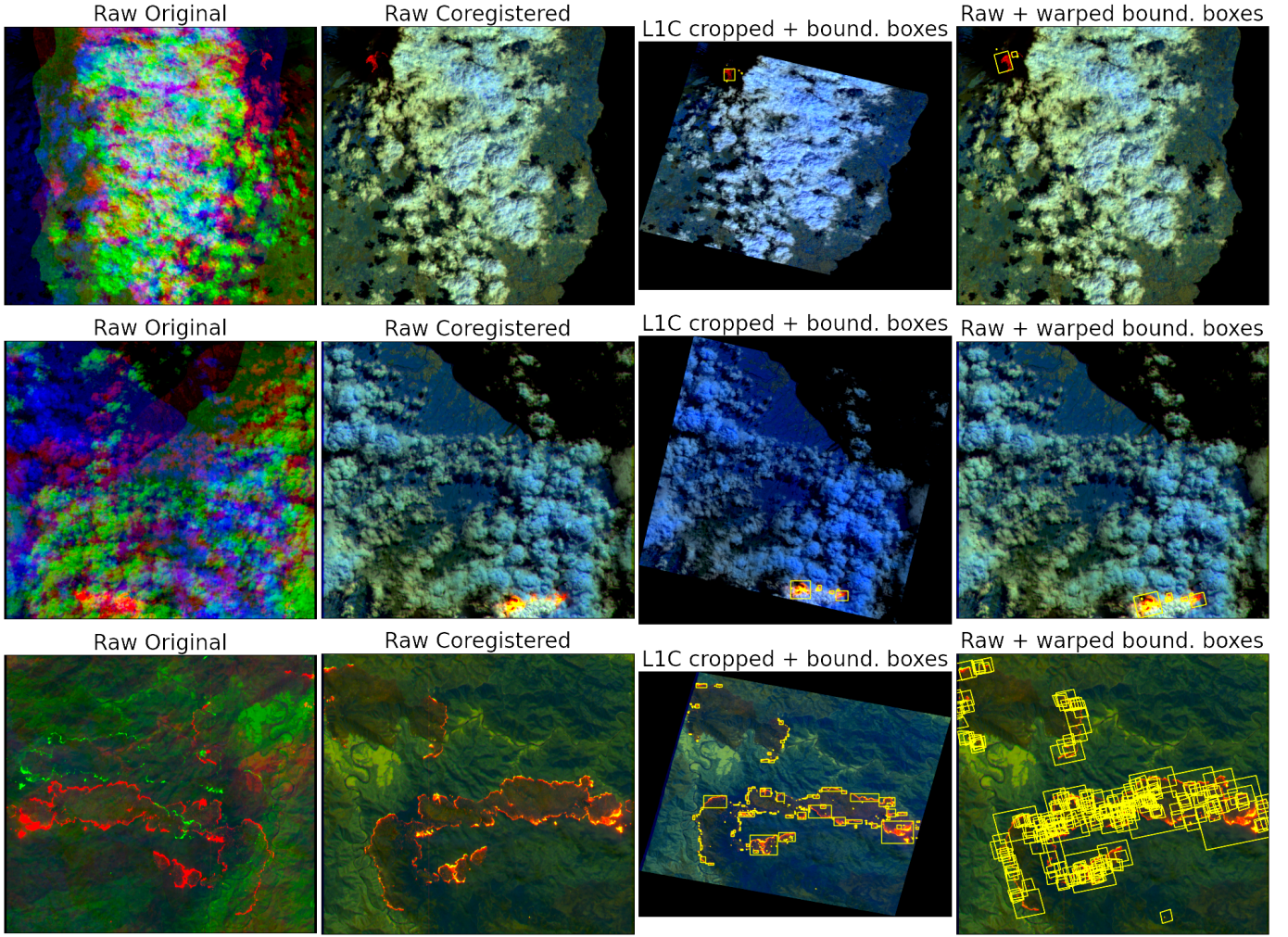


Fig. 5. Each row shows all the processing steps for various raw data granules: the first image from left of each row displays the raw data granule, the second image shows a spatially registered granule, the third image shows the correspondent L1C tiles cropped on the coordinates of first band of the raw data granule band collection with the detected bounding boxes, and the rightmost image showcases the bounding boxes warped on the raw data granules.

VII-B1. Moreover, given its different trade-offs in terms of accuracy/computational complexity, it provides an alternative solution to standard spatial registration techniques that foster the research of onboard *end-to-end* processing algorithms.

1) *Coarse coregistration methodology*: Starting from the sensor characteristics and mode of acquisition, a set of deterministic shifts between all band pairs can be determined. These shifts can be applied to perform a coarse spatial coregistration not taking into account effects due to noise or depending on the surface characteristics. In fact, these values are general for all scenes and can be empirically determined with the following methodology.

Let us consider two bands $B_{I(n)}$ and $B_{I(m)}$, with $B_{I(n)}, B_{I(m)} \in B_S$ where $B_S \triangleq [B_x, B_y, \dots, B_z]$ is the band collection of a granule that we want to spatially register. To perform the CSC, we apply a shift along and across satellite-track $\overline{S_{B_{I(n)}-B_{I(m)}}}$ to the band $B_{I(n)}$ measured with respect to the resolution of $B_{I(m)}$. $\overline{S_{B_{I(n)}-B_{I(m)}}}$ depends only on the couple of bands $(B_{I(n)}, B_{I(m)})$, the satellite and the number of detector producing that raw data (detector number).

For any corner case (i.e., satellite, detector number) $\overline{S_{B_{I(n)}-B_{I(m)}}$ can be calculated by using the relations in Eq. 3:

$$\begin{cases} \overline{S_{B_{I(n)}-B_{I(m)}}} = \sum_{k=m}^n N_{I(k+1)-I(k)} \cdot \frac{R_{B_{I(k+1)}}}{R_{B_{I(n)}}}, & n > m \\ \overline{S_{B_{I(n)}-B_{I(m)}}} = -\overline{S_{B_{I(m)}-B_{I(n)}}} \cdot \frac{R_{B_{I(n)}}}{R_{B_{I(m)}}}, & n < m \end{cases} \quad (3)$$

where $R_{B_{I(k+1)}}$ is the resolution in m of the band $B_{I(k+1)}$, and $N_{I(k+1)-I(k)}$ is the shift to apply to the band $B_{I(k)}$ to match the band $B_{I(k+1)}$ measured with respect to the resolution of the band $B_{I(k)}$.

Given a certain corner case, $N_{I(k+1)-I(k)}$ are fixed coefficients that we estimated for the each of the couples $(B_{I(k)}, B_{I(k+1)})$. To measure the coefficients $N_{I(k+1)-I(k)}$ we used the methodology described in Sec. VI-B2.

2) *SuperGlue for coarse spatial coregistration*: SuperGlue [34] is exploited as a powerful and robust solution for key-points matching from image pairs in order to measure the along-track and across-track distance of two adjacent spectral

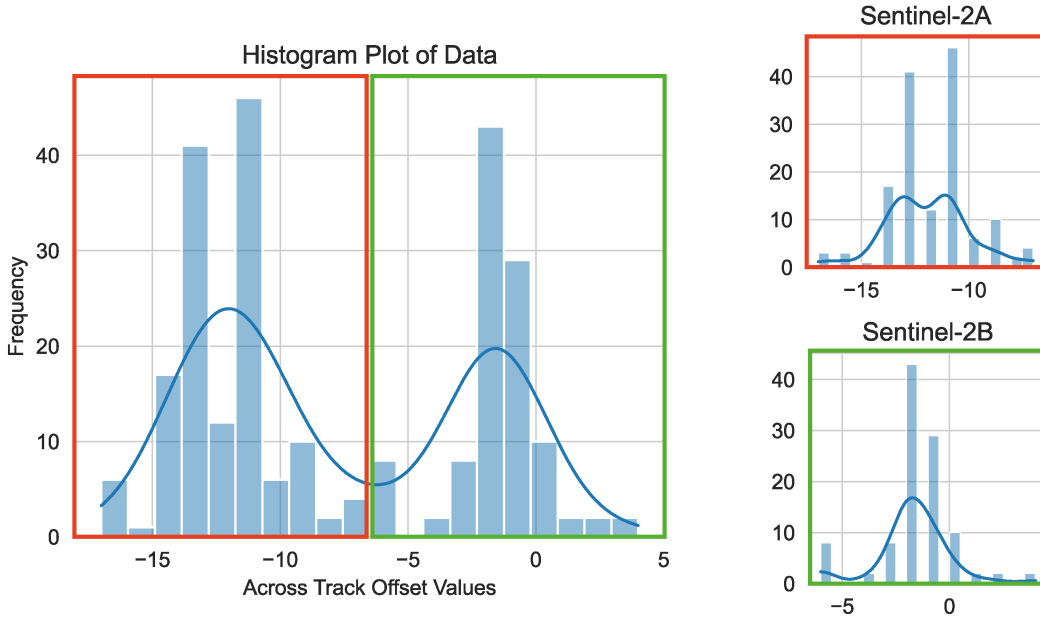


Fig. 6. Histograms of across-track offset values for all satellites (left panel), Sentinel-2A (right-top panel) and Sentinel-2B (right-bottom panel). [B8A-B11 bands]

bands. The process is iterated for each pair of bands. SuperGlue is a middle-end Neural Network designed to solve the keypoints matching problem for complex geometric computer vision tasks such as Simultaneous Localization and Mapping (SLAM) and Structure-from-Motion (SfM). With middle-end, the authors of [34] indicate that any backbone may be used as a prior feature extractor (front-end). Traditionally, local feature matching is performed by detecting interest points, computing visual descriptors, matching these with a Nearest Neighbor (NN) approach, and filtering incorrect matches. Contrarily, SuperGlue adopts a unique method by executing context aggregation, matching, and filtering concurrently within a single end-to-end architecture. Its ability to handle partial visibility and occlusion, its use of graph neural network and attention, and its flexibility and efficiency make it a great tool over existing other techniques. In this context, SuperGlue utilizes the Superpoint backbone as a feature extractor with outdoor weights as in the original implementation [34].

To boost feature presence and distinctiveness without introducing noise in the processing chain, as a pre-processing we use a Contrast Limited Adaptive Histogram Equalization (CLAHE) [35] algorithm. Then, SuperGlue extracts and matches keypoints from the two image pairs, i.e., the two spectral bands under analysis. It is worth highlighting that to further increase the detection and matching capabilities, we tune the hyper-parameters for our problem as reported in Table I. As one can observe, the keypoints presence has been increased along with the matching threshold. This tuning is devoted to increasing the number of strongly matched keypoints, i.e., keypoints having higher probabilities of being the same in both pictures. In the end, as a post-processing step, we remove the outliers ($\pm 2\sigma$) and average the values for both along and across track offsets.

To determine the coefficients $N_{I(k+1)-I(k)}$, we first coupled

TABLE I
SUPERGLUE HYPER-PARAMETERS CONFIGURATION FOR KEYPOINT MATCHING OF TWO CLOSE SPECTRAL BANDS

Feature Extractor	Parameter	Value
	Backbone	SuperPoint
	keypoints_threshold	0.25
	nms_radius	4
	weights	outdoor
SuperGlue	Parameter	Value
	sinkhorn_iterations	30
	match_threshold	0.75
	max_keypoints	1024

all the granules that could be stacked along the satellite track. This was done to be sure that keypoints that are located in adjacent granules could be matches successfully. Then, we ran the SuperGlue method to extract the various coefficients for each consecutive couple of bands ($B_{I(k)}, B_{I(k)}$) on the volcano dataset without excluding not useful granules. For each couple of bands, we used the mean value of $N_{I(k+1)-I(k)}$ was measured as the mean of shifts extracted by SuperGlue over the couples of granules having the same satellite and detector number.

Since no granule among the volcano events was generated by detector number 6, to measure $N_{I(k+1)-I(k)}$ we used the methodology on the final database.

However, we found that band B_{10} was difficult to correlate with the bands B_{03} and B_{04} because of the significant difference in the spectral content. This makes the estimated values of N_{04-10} and N_{10-03} unreliable. To solve this problem, we extracted two additional coefficients N_{10-09} and N_{10-03} and used them to invert Eq. 3 and provide better estimates for N_{04-10} and N_{10-03} . The extraction of N_{10-09} was possible because of the higher correlation of the spectral contents of

the bands B_{10} and B_{09} .

C. Raw data granules georeferencing

The band georeferencing scheme developed in this study is optimized for onboard satellite applications, and it is based on the utilization of fixed band-to-band shifts of granule corner coordinates to geolocate the corners of each band. This approach allows for an efficient georeferencing of each point within a band maintaining a balance between efficiency and accuracy. We begin by extracting the four corner coordinates of a granule, which is fundamental ancillary information detailed in the Sentinel-2 raw product metadata. The latter reported in terms of latitude and longitude in the *EPSG:4326* reference system, cannot directly be used for each band due to the aforementioned issue of inter-band shifts. The devised method employs the coarse-estimated offsets from band B02 serving as the reference. The *Prior Coordinates* are prompted as offsets from the priors coordinates of the reference band. The resulting prior coordinates are then used, in conjunction with additional information, e.g. the granule length and spatial resolution of the band, to determine the *Afterward Coordinates*. Additionally, it is essential to note that, given the variations in spatial resolution between bands, the shifts are scaled specifically for each band.

D. LIC processing

1) *LIC mosaicing and cropping*: After computing the coordinates of the various bands of the band collection B_S of a granule, it is now possible to retrieve the area covered by the spatially registered band collection on LIC products. Since the bands are spatially registered, the area of interest matches one of the first bands in B_S , with the eventual discharge of the pixels left empty by the shifting process if no filler elements are available from adjacent granules.

To retrieve the same area on the LIC products, for each band B_x in B_S , we extract and collate the correspondent band in each of the LIC tiles that intersect the polygon used to download granules. The resulting mosaic is, then, cropped on the AOI by using the geographical coordinates retrieved by using the process described in Sec. VI-C. It is worth noting that before cropping the LIC products must be re-projected into the raw coordinates reference system (*EPSG : 4326*). Finally, the cropped mosaic of the various bands are resampled to match the band having the coarsest resolution.

2) *Warm temperature hotspot detection on LIC tile*: To detect thermal hotspots, we used a simplified implementation of [28] to generate a hotmap containing thermal hotspots and extract bounding boxes. In particular, as for the original implementation, we derived a hotmap containing candidate anomalies fulfilling four logical conditions (α, β, S, γ in the original work) that are calculated by applying fixed thresholds on the ratios of TOA reflectance of the different bands.

Then, we extracted a bounding box for every cluster of pixels in the hotmap by using *scikit-image* [36]. Finally, to minimise the false detection rate, we filtered those bounding boxes surrounding a number of active pixels in the hotmap lower than 9 to discard small clusters of pixels as suggested in [28].

In the original implementation, the authors extract statistical information related to each cluster of pixels to set cluster-dependent thresholds to reduce the false positive rate. In our implementation, we omitted this step since we are not interested in pixel-level information, but the creation of a hotmap is used only for binary classification and bounding boxes extraction.

The work by Massimetti et al. [28] was originally implemented for volcanic eruption. However, other works such as [37] consider volcanic eruptions and wildfires as thermal anomalies using the same Sentinel-2 bands and threshold-based detection methods. Given the methodological similarity, we used the approach of [28] also to detect fire events in LIC tiles.

E. Bounding box warping on raw data granules

It is important to note that the bounding boxes as extracted from the LIC products cannot be straightforwardly used for the raw data due to their different projections. While the raw products are represented in azimuth-range coordinates (*EPSG : 4326*), LIC products are in latitude-longitude projected in the *WGS84* system. A further issue is added by the geometrical correction applied to the LIC images, in which a resampling using a 90m DEM (PlanetDEM 90)⁶ is employed. In order to exploit the LIC bounding boxes, we warp the points from the LIC to the raw coordinates with an affine transformation. We define the transformation matrix from LIC to raw coordinates using the coordinates of three corner points. After applying the correction, our results show that in several cases there still exists a discrepancy between the bounding box and the actual event. In order to rectify the issue, we manually tuned the bounding boxes for eruptions and create a buffer for fire events.

VII. RESULTS

A. Dataset results

As detailed in Table II, the THRawS dataset comprises a collection of 58 volcanic eruptions, 20 fire events, and 10 not-events, for a total of 88 elements.

It is important to notice that to each of the 88 elements it corresponds to one or more than *useful granules*, which has been appropriately annotated with corresponding bounding boxes if the granule contains a specific event. Therefore, the total number of *useful granules* in the THRAWS dataset is 153, of which 90 correspond to volcanic eruptions, 52 to fire events, and 11 granules depict the volcanic areas where no eruptions were observed. The remaining granules showcase other areas such as forests, lands, or other areas that do not feature any specific characteristics or hotspots.

⁶Reference Document: GMES-GSEG-EOPG-TN-09-0029 (v2.3)

TABLE II
DATASET DESCRIPTION IN TERMS OF RAW PRODUCTS AND USEFUL GRANULES

Product / Event	Eruption	Fire	Not-Event
raw Products	58	20	10
raw Useful Granules	90	52	11

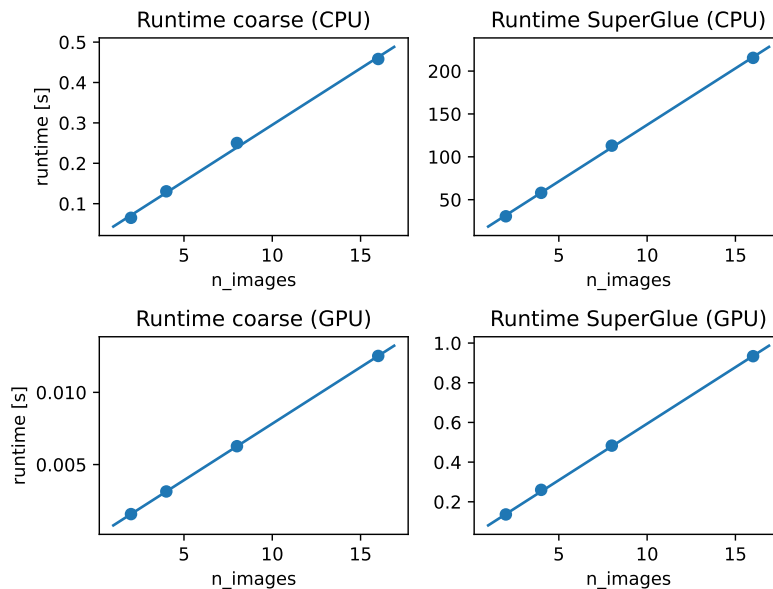


Fig. 7. Timing performance of the proposed spatial coregistration approaches vs a method based on SuperGlue on CPU (Intel(R) Xeon(R) CPU E5-2650L v4 @ 1.70GHz) and GPU (NVIDIA RTX 2080 TI).

TABLE III
MEAN AND STANDARD DEVIATION (ALONG- AND ACROSS-TRACK) OF
OFFSETS VALUES FOR EACH DETECTOR OF SENTINEL-2 OPTICAL
IMAGERS. (B8A-B11 SPECTRAL BANDS)

D	Sentinel-2A		Sentinel-2B	
	Mean	Std	Mean	Std
1	[-174.8, -1.93]	[1.01, 0.26]	[-178.33, -12.78]	[1.12, 0.44]
2	[188.0, -6.0]	[0.76, 0.0]	[186.83, -16.5]	[1.47, 0.55]
3	[-173.08, -2.0]	[0.79, 0.0]	[-174.77, -13.0]	[1.42, 0.0]
4	[186.0, -3.2]	[0.94, 0.42]	[183.22, -14.06]	[0.94, 0.24]
5	[-170.5, -1.88]	[0.53, 0.35]	[-172.5, -13.0]	[0.62, 0.0]
6	[184.0, -2.0]	[0.0, 0.0]	[183.0, -12.75]	[0.82, 0.5]
7	[-170.0, -1.0]	[0.0, 0.0]	[-173.0, -11.67]	[0.0, 0.58]
8	[185.56, -0.64]	[1.12, 0.49]	[184.12, -10.96]	[0.83, 0.2]
9	[-170.55, -1.73]	[1.04, 0.47]	[-172.6, -11.0]	[0.82, 0.0]
10	[187.0, 1.5]	[0.0, 0.58]	[185.13, -9.33]	[0.83, 0.49]
11	[-176.0, -0.5]	[0.0, 0.71]	[-174.88, -11.88]	[1.13, 0.35]
12	[193.0, 4.0]	[0.0, 0.0]	[189.17, -7.33]	[0.41, 0.52]

It is crucial to highlight that the problem of detecting fires, in particular, should be evaluated as a semantic segmentation problem. However, in the present preliminary application, the dataset has been provided with bounding boxes and thus the problem is approached as an object detection task. This approach is necessitated by the challenge of obtaining segmentation masks for raw data products. Some examples of raw data available in the dataset in the various processing steps are shown in Fig. 5.

B. Coregistration study results

The present section comprises an analysis of the results obtained from the numerical study conducted on the reported dataset. It is pertinent to highlight that value of the spatial shift were retrieved by using the datasets including only volcanoes events and not-events prior to the filtering of raw data granules. Instead, the current study goes beyond the aforementioned

focus area by testing the robustness of the approach across the entire post-processed dataset, also including fire events.

1) *Coarse spatial registration: algorithmic performance:* Concerning the accuracy, Table III is a good indicator presenting the mean and standard deviation of the across- and along-track offsets for the B8A-B11 spectral bands. Such values were obtained by measuring the error due to the proposed CSC method with respect to the shifts that one can obtain by using the SuperGlue method, as suggested in Section VI-B2. Notably, the standard deviation values exhibit a general trend of being below one pixel for both along- and across-track directions. Although this behaviour has been reported for only the B8A-B11 spectral bands, it is essential to note that this trend has been consistently verified for each spectral band pair of the Sentinel-2 images. Also note that the results presented in the table have been differentiated based on the satellite and detector number.

This differentiation based on the satellite and detector number is necessary due to the empirical observation of dependence on the satellite. As an example, focusing on the B8A-B11 spectral bands, the accompanying histogram of across-track offsets illustrated in Figure 6 highlights a bimodal distribution. It is noteworthy that these curves are attributed to the Sentinel-2A and Sentinel-2B satellites, with greater offset values laying for Sentinel-2A (marked in red). This behaviour could be due to the eventual improvements applied to the detectors of Sentinel-2 B satellite with respect to its predecessor, Sentinel-2 A.

Furthermore, an additional interesting pattern that is observable in the results is a change in sign when transitioning from odd to even detectors. This pattern is attributed to the fact that the detectors are inverted on the satellite, which results in an opposite offset sign for even detectors as compared to odd detectors.

2) *Coarse spatial registration: timing performance:* The findings of the present study showcase the potential of the proposed implementation, which significantly minimises the amount of time and effort required for the co-registration of a given product.

To assess the advantage in terms of timing of the coarse spatial coregistration, we set up an experiment to compare the time to register a certain number of raw data granules by using fixed pre-calculated shifts to the approach based on SuperGlue, which optimises the shift value for each band of each raw data granule. More specifically, for both the methods we measured the time to register the bands B_{8A}, B_{11}, B_{12} for 2, 4, 8, 16 raw data granules in a row. We profiled both the methods by using PyTorch Profiler [38] both on an Intel(R) Xeon(R) CPU E5-2650L v4 @ 1.70GHz CPU and an NVIDIA RTX 2080 TI GPU to test the dependency on the time performance on the hardware device. Each test case was run three times and time performances were measured by averaging the results on the three test with the same number of raw data granules. All the tests were performed continuously with two warm-up cycles at the beginning of the test series with one raw data granules. Precalculated shifts were stored in memory to reduce the overhead time due to the storage memory access when coarse spatial coregistration was used. When SuperGlue was used, shift values were retrieved by using the approach and the model set-up described in Section VI-B2. A dedicated inference of the SuperGlue network was needed for each couple of bands to be registered, since the implementation provided [39] processes only couple of images but not support processing with higher batch size.

Results are shown in Fig 7. On both the devices, both the methods show a linear increment of the time to perform the bands registration with the number of images. On CPU, the time required by the method relying on SuperGlue requires averagely 471x the time required by the method with precalculated coefficients, whilst on GPU this ratio decreases to an average 72x.

In particular, the methodology with fixed shifts requires respectively 0.028s and 0.78 ms on CPU for a raw data granule with bands B_{8A}, B_{11}, B_{12} , demonstrating to be a really lightweight methodology.

VIII. CONCLUSION

For the very first time, a dataset comprising uncompressed Sentinel-2 datasets data for the detection of warm temperature hotspots was presented in this paper. The THRawS dataset has a collection of 88 elements between volcanic, fire events and not-events that correspond to more than 100+ *useful granules*. It will allow researchers to experiment with and create novel applications and approaches for finding warm temperature hotspots using raw satellite images. Furthermore, the dataset contains a collection of eventless granules that may be used for both warm-event detection and general classification applications.

The proposed algorithm for geo-referencing and coregistering decompressed bands of interest in raw data granules was found to be robust throughout the full dataset. These

algorithms, the mosaicking and cropping of the bands of the appropriate L1C tiles, and the identification of thermal anomalies using traditional algorithms were all part of the strategy for gaining a labeled dataset of raw Sentinel-2 data.

The study also compared the suggested “coarse-coregistration” strategy to the SuperGlue Deep Neural Network method in terms of performance, which was taken as a baseline solution that optimises the spatial shifts for every single couple of bands of an raw data granule. The results revealed that the proposed spatial coarse coregistration is capable to keep registration errors with standard deviations between 0 and 1.47 px for the various detectors while offering a lightweight solution that can be implemented in ms on the tested hardware. This demonstrates that the suggested “coarse spatial-coregistration” approach is light and should be further explored for onboard applications.

In essence, the present work illustrates a unique method to produce Sentinel-2 raw datasets, applied on the detection of warm temperature hotspots, and suggests a lightweight methodology to process such data that can be studied in future works exploiting AI models for onboard applications.

IX. GLOSSARY

In order to ensure the clarity and consistency of the current paper, a glossary including the technical terms defined uniformly across the document is provided, making it easier for readers to have a deeper understanding of the content.

- **Raw data Granule:** Raw data granule refers to a specific type of data produced in the processing chain of Sentinel-2, as described in Sec. II-C. Raw data granules are obtained from the decompression applied to the L0 data with additional data, which are then further processed to obtain radiometrically calibrated radiances in L1B products, and finally, after geometric corrections, to obtain TOA reflectances in L1C products.
- **Useful Granule:** a raw granule for which band B_x (B_{8A} for our goal) includes at least a bounding box, obtained through the processing described in Sec. VI. The definition of Useful granules depends on the band collection used and, therefore, on the reference L1C algorithms used to retrieve the events of interest,
- **Coarse Spatial Co-Registration:** band spatial coregistration technique that compensates only the physical shift due to pushbroom nature of the sensor.
- **Prior coordinates:** first two corner coordinates as scanned by the pushbroom system.
- **Afterward coordinates:** last two corner coordinates as scanned by the pushbroom system.

X. DATA AVAILABILITY

The dataset associated with this study is available and can be accessed through the following DOI: [10.5281/zenodo.7908728](https://doi.org/10.5281/zenodo.7908728). In addition to the dataset itself, supplementary materials such as code scripts, data dictionaries, or documentation may also be available through the repository (PyRaws: <https://github.com/ESA-PhiLab/>) to facilitate understanding and replication of the research.

REFERENCES

- [1] G. Furano, G. Meoni, A. Dunne, D. Moloney, V. Ferlet-Cavrois, A. Tavoularis, J. Byrne, L. Buckley, M. Psarakis, K.-O. Voss *et al.*, "Towards the use of artificial intelligence on the edge in space systems: Challenges and opportunities," *IEEE Aerospace and Electronic Systems Magazine*, vol. 35, no. 12, pp. 44–56, 2020.
- [2] K. Thangavel, D. Spiller, R. Sabatini, P. Marzocca, and M. Esposito, "Near real-time wildfire management using distributed satellite system," *IEEE Geoscience and Remote Sensing Letters*, vol. 20, pp. 1–5, 2023.
- [3] L. Diana, J. Xu, and L. Fanucci, "Oil spill identification from sar images for low power embedded systems using cnn," *Remote Sensing*, vol. 13, no. 18, p. 3606, 2021.
- [4] P. Di Stasio, A. Sebastianelli, G. Meoni, and S. L. Ullo, "Early detection of volcanic eruption through artificial intelligence on board," in *2022 IEEE International Conference on Metrology for Extended Reality, Artificial Intelligence and Neural Engineering (MetroXRINE)*. IEEE, 2022, pp. 714–718.
- [5] M. P. Del Rosso, A. Sebastianelli, D. Spiller, P. P. Mathieu, and S. L. Ullo, "On-board volcanic eruption detection through cnns and satellite multispectral imagery," *Remote Sensing*, vol. 13, no. 17, p. 3479, 2021.
- [6] G. Mateo-Garcia, J. Veitch-Michaelis, L. Smith, S. V. Oprea, G. Schumann, Y. Gal, A. G. Baydin, and D. Backes, "Towards global flood mapping onboard low cost satellites with machine learning," *Scientific Reports*, vol. 11, no. 1, p. 7249, Mar. 2021, number: 1 Publisher: Nature Publishing Group. [Online]. Available: <https://www.nature.com/articles/s41598-021-86650-z>
- [7] M. Kerr, S. Cornara, and A. Ramirez, "Intelligence and autonomy in the sat4eo+ satellite," 2021.
- [8] V. Růžicka, A. Vaughan, D. De Martini, J. Fulton, V. Salvatelli, C. Bridges, G. Mateo-Garcia, and V. Zantedeschi, "RaVÆn: unsupervised change detection of extreme events using ML on-board satellites," *Scientific Reports*, vol. 12, no. 1, p. 16939, Oct. 2022, number: 1 Publisher: Nature Publishing Group. [Online]. Available: <https://www.nature.com/articles/s41598-022-19437-5>
- [9] G. Giuffrida, L. Fanucci, G. Meoni, M. Batič, L. Buckley, A. Dunne, C. van Dijk, M. Esposito, J. Hefele, N. Vercruyssen, G. Furano, M. Pastena, and J. Aschbacher, "The ϕ -sat-1 mission: The first on-board deep neural network demonstrator for satellite earth observation," *IEEE Transactions on Geoscience and Remote Sensing*, vol. 60, pp. 1–14, 2022.
- [10] G. Guerrisi, F. Del Frate, and G. Schiavon, "Convolutional autoencoder algorithm for on-board image compression," in *IGARSS 2022-2022 IEEE International Geoscience and Remote Sensing Symposium*. IEEE, 2022, pp. 151–154.
- [11] M. B. Henriksen, J. L. Garrett, E. F. Prentice, A. Stahl, T. A. Johansen, and F. Sigernes, "Real-time corrections for a low-cost hyperspectral instrument," in *2019 10th Workshop on Hyperspectral Imaging and Signal Processing: Evolution in Remote Sensing (WHISPERS)*, 2019, pp. 1–5.
- [12] M. Drusch, U. Del Bello, S. Carlier, O. Colin, V. Fernandez, F. Gascon, B. Hoersch, C. Isola, P. Laberinti, P. Martimort, A. Meygret, F. Spotó, O. Sy, F. Marchese, and P. Bargellini, "Sentinel-2: ESA's optical high-resolution mission for GMES operational services," *Remote Sensing of Environment*, vol. 120, pp. 25–36, 2012, the Sentinel Missions - New Opportunities for Science. [Online]. Available: <https://www.sciencedirect.com/science/article/pii/S0034425712000636>
- [13] J. A. Richards and J. A. Richards, *Remote sensing digital image analysis*. Springer, 2022, vol. 5.
- [14] "Sentinel-2 Products Specification Document," Available online at: <https://sentinel.esa.int/documents/247904/685211/sentinel-2-products-specification-document>, last accessed on 21st January 2023.
- [15] ESA, "S2-pdgs-mpc-atbd-11," ESA, Tech. Rep., 2022. [Online]. Available: <https://sentinels.copernicus.eu/documents/247904/446933/Sentinel-2-Level-1-Algorithm-Theoretical-Basis-Documents-ATBD.pdf>
- [16] M. Shah, M. S. Raval, and S. Divakaran, "A deep learning perspective to atmospheric correction of satellite images," in *IGARSS 2022 - 2022 IEEE International Geoscience and Remote Sensing Symposium*, 2022, pp. 346–349.
- [17] "Sentinel Online - Calibration," Available online at: <https://sentinels.copernicus.eu/web/sentinel/technical-guides/sentinel-2-msi/calibration>, last accessed on 04 March 2023.
- [18] D. Derksen, G. Meoni, G. Lecuyer, A. Mergy, M. Märtens, and D. Izzo, "Few-shot image classification challenge on-board," in *Workshop-Data Centric AI, NeurIPS*, 2021.
- [19] "AI on the edge: "the OPS-SAT case"," Available online at: <https://kelvins.esa.int/opssat/>, last accessed on 06 March 2023.
- [20] "OPS-SAT," Available online at: https://www.esa.int/Enabling_Support/Operations/OPS-SAT, last accessed on 20 February 2023.
- [21] M. Tan and Q. Le, "Efficientnet: Rethinking model scaling for convolutional neural networks," in *International conference on machine learning*. PMLR, 2019, pp. 6105–6114.
- [22] G. Mateo-García, J. Veitch-Michaelis, C. Purcell, N. Longepe, P. P. Mathieu, S. Reid, A. Anlind, F. Bruhn, and J. Parr, "In-orbit demonstration of a re-trainable machine learning payload for processing optical imagery," 2022.
- [23] A. S. Danielsen, T. A. Johansen, and J. L. Garrett, "Self-organizing maps for clustering hyperspectral images on-board a cubesat," *Remote Sensing*, vol. 13, no. 20, p. 4174, 2021.
- [24] P. Helber, B. Bischke, A. Dengel, and D. Borth, "EuroSAT: A novel dataset and deep learning benchmark for land use and land cover classification," *IEEE Journal of Selected Topics in Applied Earth Observations and Remote Sensing*, vol. 12, no. 7, pp. 2217–2226, 2019.
- [25] "Global Volcanism Program, 2022. [Database] Volcanoes of the World (v. 5.0.1; 19 Dec 2022). Distributed by Smithsonian Institution, compiled by Venkze, E. <https://doi.org/10.5479/si.GVP.VOTW5-2022.5.0>," Available online at: https://volcano.si.edu/search_eruption.cfm, last accessed on 28 December 2022.
- [26] P. L. Abbott, *Natural Disasters*, 6th ed. New York: McGraw-Hill Higher Education, 2008.
- [27] N. Andela, J. W. Kaiser, G. R. van der Werf, and M. J. Wooster, "New fire diurnal cycle characterizations to improve fire radiative energy assessments made from modis observations," *Atmospheric Chemistry and Physics*, vol. 15, no. 15, pp. 8831–8846, 2015. [Online]. Available: <https://acp.copernicus.org/articles/15/8831/2015/>
- [28] F. Massimetti, D. Coppola, M. Laiolo, S. Valade, C. Cigolini, and M. Ripepe, "Volcanic hot-spot detection using sentinel-2: A comparison with modis-mirova thermal data series," *Remote Sensing*, vol. 12, no. 5, 2020. [Online]. Available: <https://www.mdpi.com/2072-4292/12/5/820>
- [29] R. Binet, E. Bergsma, and V. Poulain, "Accurate sentinel-2 inter-band time delays," *ISPRS Annals of Photogrammetry, Remote Sensing & Spatial Information Sciences*, no. 1, 2022.
- [30] P. E. Anuta, "Spatial registration of multispectral and multitemporal digital imagery using fast fourier transform techniques," *IEEE transactions on Geoscience Electronics*, vol. 8, no. 4, pp. 353–368, 1970.
- [31] P. Nandy, B. N. Post, J. L. Smith, and M. L. Decker, "Edge-based correlation image registration algorithm for the multispectral thermal imager (mti)," in *Algorithms and Technologies for Multispectral, Hyperspectral, and Ultraspectral Imagery X*, vol. 5425. SPIE, 2004, pp. 197–207.
- [32] R. Kennedy and W. Cohen, "Automated designation of tie-points for image-to-image coregistration," *International Journal of Remote Sensing*, vol. 24, no. 17, pp. 3467–3490, 2003.
- [33] G. Yu, T. Vladimirova, and M. Sweeting, "Autonomous band registration for on-board applications," in *2007 IEEE International Conference on Signal Processing and Communications*, 2007, pp. 1327–1330.
- [34] P.-E. Sarlin, D. DeTone, T. Malisiewicz, and A. Rabinovich, "Superglue: Learning feature matching with graph neural networks," in *Proceedings of the IEEE/CVF conference on computer vision and pattern recognition*, 2020, pp. 4938–4947.
- [35] P. Musa, F. Al Rafi, and M. Lamsani, "A review: Contrast-limited adaptive histogram equalization (clahe) methods to help the application of face recognition," in *2018 third international conference on informatics and computing (ICIC)*. IEEE, 2018, pp. 1–6.
- [36] "scikit-image," Available online at: <https://scikit-image.org/>, last accessed on 31st January 2023.
- [37] Y. Liu, W. Zhi, B. Xu, W. Xu, and W. Wu, "Detecting high-temperature anomalies from Sentinel-2 MSI images," *ISPRS Journal of Photogrammetry and Remote Sensing*, vol. 177, pp. 174–193, 2021. [Online]. Available: <https://www.sciencedirect.com/science/article/pii/S0924271621001337>
- [38] "PyTorch Profiler," Available online at: https://pytorch.org/tutorials/recipes/recipes/profiler_recipe.html, last accessed on 13 February 2023.
- [39] "SuperGlue Inference and Evaluation Demo Script," Available online at: <https://github.com/magicLeap/SuperGluePret>, last accessed on 13 February 2023.